Energy Storage Materials 48 (2022) 356–365

Contents lists available at ScienceDirect

Energy Storage Materials

journal homepage: www.elsevier.com/locate/ensm

A high-performance intermediate-temperature aluminum-ion battery based on molten salt electrolyte

Kuangyu Wang[a], Kai Liu[b,*], Cheng Yang[c], Ziyao Chen[a], Haitian Zhang[d], Yulong Wu[a], Yuanzheng Long[a], Yang Jin[e], Xiangming He[d], Meicheng Li[b], Hui Wu[a,*]

[a] State Key Lab of New Ceramics and Fine Processing, School of Materials Science and Engineering, Tsinghua University, Beijing 100084, PR China
[b] State Key Laboratory of Alternate Electrical Power System with Renewable Energy Sources, School of New Energy, North China Electric Power University, Beijing 102206, PR China
[c] Center for Advanced Mechanics and Materials Applied Mechanics Laboratory, Department of Engineering Mechanics, Tsinghua University, Beijing 100084, PR China
[d] Institute of Nuclear and New Energy Technology, Tsinghua University, Beijing 100084, PR China
[e] Research Center of Grid Energy Storage and Battery Application, School of Electrical Engineering, Zhengzhou University, Zhengzhou 450001, PR China

ARTICLE INFO

Keywords:
Grid-scale energy storage
Aluminum-ion battery
Molten salt electrolyte
Metal sulfide

ABSTRACT

Non-aqueous rechargeable aluminum-ion batteries (AIBs) are a promising candidate for grid-scale energy storage due to their high theoretical energy density, safety, environmental benignity, and the abundance of Al sources. However, the limited cathode capacity and the high price of ionic liquid electrolytes hinder their large-scale applications. Herein, an intermediate-temperature AIB composed of nickel disulfide-based cathode and NaCl-$AlCl_3$-Al_2S_3 molten salt electrolyte is reported. A highly reversible conversion mechanism between Ni_3S_4 and Ni during cycling is proved with cathode capacities exceeding 500 mAh g^{-1}. The full cell delivers a cathode capacity of 320 mAh g^{-1} at 240 °C and a current density of 2000 mA g^{-1} with negligible capacity fade after 2000 cycles. The raw material cost is estimated to be as low as 28 \$ kWh^{-1} based on the electrode and electrolyte materials. The molten salt electrolyte-based AIB provides promising opportunities to build energy storage systems with low cost, high safety, stable electrochemical performance, and long lifetime.

1. Introduction

Grid-scale energy storage is critical for renewable energy integration, and there is a desire to develop new electrochemical energy storage systems with high safety, low cost, and competitive energy density to fit the increasing requirements of large-scale applications [1]. In the past decades, lithium-ion batteries have achieved enormous success in energy storage applications [2]. However, researchers have to seek more sustainable battery systems considering the high cost, safety concerns, and recycling problems of lithium-based batteries [3,4]. In this regard, batteries based on sodium, magnesium, and aluminum have attracted much attention [5–8]. Among them, aluminum-ion batteries (AIBs) possess the potential to achieve high energy density and low energy cost due to the competitive specific capacity (2978 mAh g^{-1}) and low price (~2.6 \$ kg^{-1}) of aluminum [9]. Additionally, the high stability and safety of the metallic aluminum electrode make it much more preferable for battery manufacturing than the metallic lithium electrode [10].

AIBs can be classified into aqueous and non-aqueous systems based on the compositions of the electrolyte [11]. Aqueous electrolytes own lower cost and higher ionic conductivity but are limited by the narrow electrochemical stability window [12,13]. Recently, significant progress has been made with respect to non-aqueous AIBs with room-temperature ionic liquid (IL) electrolytes and carbon-based cathodes [8,14-16]. Although the battery system demonstrates good rate performance and cycling stability, the high cost of IL electrolytes and the relatively low capacity of carbon-based cathodes challenge their practical applications [17]. As a result, metal sulfides such as nickel sulfides [18,19], molybdenum sulfides [20,21], cobalt sulfides [22,23], and vanadium sulfides [24,25], have been investigated as alternative cathode materials because of their potential to achieve higher capacities [26,27]. However, there is a large disparity between the cell-level capacities and their theoretical values due to the poor conductivity and the structural instability of such materials [17,28]. Moreover, the cathodes are synthesized at the nanoscale level with limited active material loadings of less than 3 mg cm^{-2} in most cases [19-23,29-30]. Further research on cost-effective electrode synthesis routes suitable for mass production is required before real applications.

Herein, we report an intermediate-temperature aluminum-nickel disulfide battery (Al/NiS_2 battery) with molten salt electrolyte. The NiS_2@carbon black (NiS_2@C) cathode is prepared by an in-situ molten salt synthesis method with an ultrahigh active material loading of 30 mg

* Corresponding authors.
E-mail addresses: liukai21@ncepu.edu.cn (K. Liu), huiwu@tsinghua.edu.cn (H. Wu).

https://doi.org/10.1016/j.ensm.2022.03.030
Received 23 November 2021; Received in revised form 23 February 2022; Accepted 18 March 2022
Available online 23 March 2022

cm^{-2}. Taking advantage of the high ionic conductivity of the NaCl-$AlCl_3$-Al_2S_3 electrolyte (~0.39 S cm^{-1} at 180 °C, comparable to ~0.02 S cm^{-1} for $AlCl_3$-[EMI*m*]Cl at room temperature) [31,32], as well as the fast reaction kinetics at elevated temperatures [33], a superior cathode capacity of over 500 mAh g^{-1} is obtained. The Al/NiS_2 battery system presents excellent cycling stability and rate capability in a relatively wide working temperature window, delivering a cathode capacity of 380 mAh g^{-1} after 1000 cycles at 180 °C and a current density of 1000 mA g^{-1} and a cathode capacity of 320 mAh g^{-1} after 2000 cycles at 240 °C and a current density of 2000 mA g^{-1}. Meanwhile, the cell can tolerate repeated overcharges and recover after being cooled down to ambient temperature, ensuring stable operations with easy maintenance in practical application environments.

2. Material and methods

2.1. Materials

NaCl, $AlCl_3$, S, $NiCl_2$, Al, polytetrafluoroethylene (PTFE) preparation (60 wt% dispersion in H_2O), and alcohol used in this work were analytical reagent grade and commercially available from Aladdin Bio-Chem Technology Co., Ltd (Shanghai, China). Carbon black was purchased from Hefei Kejing Co., Ltd (Hefei, China). All chemicals were used directly without any purification. Glass microfiber filters (Whatman 934-AH) were used as separators.

2.2. Preparation of the NaCl-$AlCl_3$-Al_2S_3 electrolyte and the NaCl-$AlCl_3$ electrolyte

The NaCl-$AlCl_3$-Al_2S_3 electrolyte was prepared in an argon-filled glove box (Etelux, Lab2000). NaCl, $AlCl_3$, and S powders were fully mixed with a molar ratio of 1.05:1.0:0.12. The mixture was heated with excess aluminum to 120 °C for 10 h and 200 °C for 72 h. The NaCl-$AlCl_3$ electrolyte was prepared in the same glove box. NaCl and $AlCl_3$ were fully mixed with a molar ratio of 1.05:1.0. The mixture was heated with excess aluminum to 120 °C for 10 h and 200 °C for 24 h. Both melts were clear and colorless, with extra NaCl precipitating at the bottom of the container. The transparent upper melts were poured out carefully and collected.

2.3. Preparation of the NiS_2@C cathode and the $NiCl_2$@C cathode

The NiS_2@C cathode was prepared in three steps. Firstly, $NiCl_2$ was dissolved in an alcohol solution. Carbon black was impregnated with the solution and dried in an 80 °C oven. Secondly, the as-prepared $NiCl_2$@C was mixed with S and PTFE and processed into a thin slice as the cathode precursor. The cathode precursor was then pressed into two molybdenum meshes with a pressure of 30 MPa [34]. Thirdly, the cathode precursor was heated with the NaCl-$AlCl_3$-Al_2S_3 molten salt electrolyte at 180 °C for 4 h to be transformed into the NiS_2@C cathode through an in-situ molten salt synthesis method. The weight ratio of the applied $NiCl_2$, C, S, and PTFE was 3:1:2:0.5, and it can be calculated that the weight ratio of the NiS_2, C, and PTFE in the NiS_2@C cathode was around 2.8:1:0.5. The active material loading was around 30 mg cm^{-2}. The $NiCl_2$@C cathode was prepared in two steps. Firstly, $NiCl_2$ was dissolved in an alcohol solution. Carbon black was impregnated with the solution and dried in an 80 °C oven. Secondly, the as-prepared $NiCl_2$@C was mixed with PTFE, processed into a thin slice with a pressure of 30 MPa, and pressed into two molybdenum meshes. The weight ratio of the applied $NiCl_2$, C, and PTFE was 3:1:0.5. The active material loading was around 30 mg cm^{-2}.

2.4. Assembly of the Al/NiS_2 battery and the Al/$NiCl_2$ battery

The Al/NiS_2 battery was assembled in three steps. Firstly, glass seals were applied between the Ta wire and the stainless-steel battery case. The silicate-based glass has a melting point of 500 °C and was heated to 750 °C for 1 h in a muffle furnace (MTI) to reach the encapsulation. Secondly, the NaCl-$AlCl_3$-Al_2S_3 electrolyte (1.2 g) was filled in the Al case (1 mm thickness, ~1.5 g) and was heated to 180 °C. The Mo meshes were welded to the Ta wire, and the cathode (~1 cm^2, with active material loading of ~30 mg) was immersed into the electrolyte. The first two steps were performed in the argon-filled glove box. Finally, the battery was cooled to ambient temperature and taken out to ambient air. Laser welding was quickly applied at the threaded connection to ensure air-tightness. The assembly procedures of the Al/$NiCl_2$ battery were similar to that of the Al/NiS_2 battery, except that $NiCl_2$@C was applied as the cathode.

2.5. Characterization technique

The microstructures of the samples were analyzed by scanning electron microscopy (MERLIN Compact Zeiss). Phase identifications of the samples were analyzed using X-ray diffraction (D-Max-2500 Rigaku XRD Analyzer) and X-ray photoelectron spectroscopy with a 300 W Al Kα radiation (Amicus Budget). Raman spectra were obtained using a 532 nm laser (LabRAM HR Evolution). Element content analyses of the samples were conducted using inductively coupled plasma optical emission spectroscopy (Agilent 725 ICP-OES).

2.6. Electrochemical measurement

Assembled Al/NiS_2 batteries were tested in muffle furnaces (MTI) in ambient air. Battery performance was tested using a battery test system (LAND, 2001CT). Cyclic voltammetry measurements were conducted on an electrochemical workstation (CHI 660e) in two-electrode mode. Impedance measurements of assembled batteries were performed using a potentiostat with a frequency response analyzer (FRA) module (Metrohm Autolab).

3. Results

3.1. Battery structural and material design

Fig. 1a schematically demonstrates the Al/NiS_2 battery configuration, with a digital photo of an assembled cell shown in Fig. 1b. The Al case anode is filled with the NaCl-$AlCl_3$-Al_2S_3 molten salt electrolyte. The stainless-steel cylinder outside the anode serves as the current collector. NiS_2@C cathode is pressed into molybdenum (Mo) meshes welded to a tantalum (Ta) wire. In order to prevent short circuits, a glass fiber separator is covered on the cathode. Glass seals are applied between the cathode and anode current collector for gas tightness and electronic insulation.

According to the relevant research, the ionic conductivity of the electrolyte increases while the vapor pressure decreases with the fraction of NaCl [31]. As a result, the composition with saturated NaCl was chosen, and the working temperature of the battery system is suggested to be above 180 °C (Fig. S1). The ionic conductivity of the electrolyte was tested to be 0.39 S cm^{-1} at 180 °C and increased with the elevated temperature (Fig. S2). It is noteworthy that sulfur was reported to react with aluminum and NaCl-$AlCl_3$ melts according to Eqs. (1) and (2) and exist in the form of chain species $[AlSCl_2]_n^{n-}$ in the molten state. "$NaAlSCl_2$" is commonly used as an apparent formula [35,36].

$$2Al + 3S \rightarrow Al_2S_3 \quad (1)$$

$$Al_2S_3 + NaAlCl_4 + 2NaCl \rightarrow 3NaAlSCl_2 \quad (2)$$

The X-ray diffraction (XRD) pattern of the electrolyte at ambient temperature is shown in Fig. S3, and the peaks of $NaAlCl_4$ and Al_2S_3 were observed. The element contents of the electrolyte determined by inductively coupled plasma optical emission spectroscopy (ICP-OES) are listed

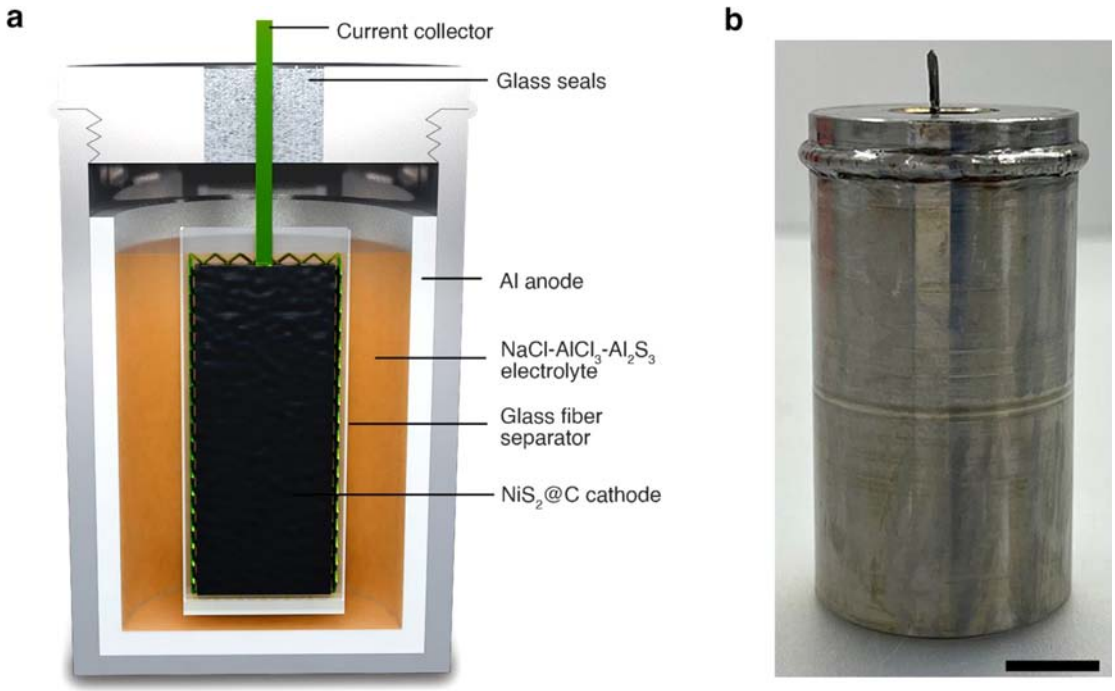

Fig. 1. Structural design of the Al/NiS_2 battery. (a) Schematic diagram of the Al/NiS_2 battery. (b) Digital photo of an assembled Al/NiS_2 battery. The scale bar is 1 cm.

in Table S1. It can be calculated that the molar ratio of NaCl, $AlCl_3$, Al_2S_3 was 1:1.03:0.03, which is reasonably consistent with the expected composition. The content of Al_2S_3 was slightly lower than expected, and it can be attributed to the H_2S volatilization through the hydrolysis reaction of Al_2S_3 during testing.

The NiS_2@C cathode was synthesized through an in-situ molten salt synthesis method. Firstly, $NiCl_2$ impregnated conductive carbon black ($NiCl_2$@C) was prepared. The $NiCl_2$@C powder was mixed with S powder and polytetrafluoroethylene (PTFE) binder and then processed into a thin slice as the cathode precursor (Fig. S4). The precursor was heated with the NaCl-$AlCl_3$-Al_2S_3 molten salt at 180 ˚C for 4 h and transformed into the NiS_2@C cathode through the following reaction.

$$NiCl_2 + S + NaAlSCl_2 \rightarrow NiS_2 + NaAlCl_4 \quad (3)$$

The scanning electron microscopy (SEM) images and the energy-dispersive X-ray (EDX) spectrum of the cathode precursor before and after being washed by deionized water are shown in Fig. 2a-2d. As seen in Fig. 2a and 2b, the surface of the precursor was covered by $NiCl_2$ with rod-like morphologies. After removing the $NiCl_2$ with deionized water, it was observed that a porous network was formed by carbon black with sulfur distributed evenly, ensuring high electrode conductivity and adequate electrolyte infiltration (Fig. 2c and 2d). The NiS_2@C cathode was also washed by deionized water to remove the electrolyte before a series of characterizations. The formation of NiS_2 was confirmed based on the XRD result in Fig. S5. SEM and the corresponding EDX spectrum (Fig. 2e and 2f) showed that the water-insoluble NiS_2 remained rod-like shapes with smaller diameters. X-ray photoelectron spectroscopy (XPS) spectra of the Ni 2p and S 2p are shown in Fig. 2g and 2h, respectively. Both the Ni $2p_{3/2}$ and the Ni $2p_{1/2}$ peaks were fitted into two spin-orbit doublets along with two satellite peaks at 861.5 and 879.0 eV. The peaks at 853.8 and 871.4 eV were attributed to Ni^{2+}, while the peaks at 856.4 and 874.0 eV were attributed to Ni^{3+}. The S 2p peak was simulated into two peaks located at 162.6 and 163.8 eV, which is consistent with the S $2p_{3/2}$ and S $2p_{1/2}$ orbitals. Meanwhile, the weak peak at 168.6 eV can be attributed to sulfur oxides on the sample surface [37]. Based on the results above, the in-situ synthesis of the NiS_2@C cathode was realized and easily integrated into the battery assembly process.

3.2. Electrochemical process and mechanisms

After assembling, the Al/NiS_2 battery was cycled at an intermediate temperature of 180 ˚C and a current density of 100 mA g^{-1} (all of the current densities of the Al/NiS_2 batteries are calculated based on the weight of NiS_2 used in cathodes). In the first discharge, three major voltage plateaus existed at 0.73 V, 0.55 V, and 0.33 V, respectively (Fig. 3a). In order to study the reaction mechanisms, three cathode samples (samples II-IV) were taken from the batteries at the end of each discharge plateau for XRD tests after being washed by deionized water to remove the electrolyte (Fig. 3b). As seen from the XRD pattern of sample II, the initial active substance NiS_2 was mostly transformed into α-NiS after the first discharge plateau. As the discharge process continued, peaks of Ni_3S_2 occurred in the XRD pattern of sample III. NiS and Ni_3S_4 were also confirmed to exist, which could be attributed to the incomplete reduction reactions. It is also worth noting that the remaining α-NiS, which is the Nickeline phase, experienced a crystal phase transformation to β-NiS, which is the Millerite phase. At the end of the first discharge, the nickel sulfide species were mainly reduced to metallic Ni. XPS tests were also conducted (Fig. S6a and Fig. S6b). The S 2p and Ni 2p peaks were nearly unchanged for samples I-III, demonstrating the existence of nickel sulfides [37–40]. The atomic ratio of S to Ni was reduced to around 1:8 for sample IV, which is consistent with the conclusion that metallic Ni served as the final discharge product. The peak at 856.1 eV can be attributed to the formation of NiO at the surface of the Ni grains [41]. Similar results were revealed by Raman spectra (Fig. S7a). The peak at 472 cm^{-1} in the spectra of sample I and the peak at 285 cm^{-1} in the spectrum of sample II corresponded to NiS_2 and NiS, respectively [42,43], while no peak was observed in the spectra of sample IV. Therefore, it can be concluded that the active substance, NiS_2, experienced multi-step reduction reactions in the first discharge as follows.

$$3NiS_2 + 3AlCl_4^- + 6e^- \rightarrow 3NiS + 3AlSCl_2^- + 6Cl^- \quad (4a)$$

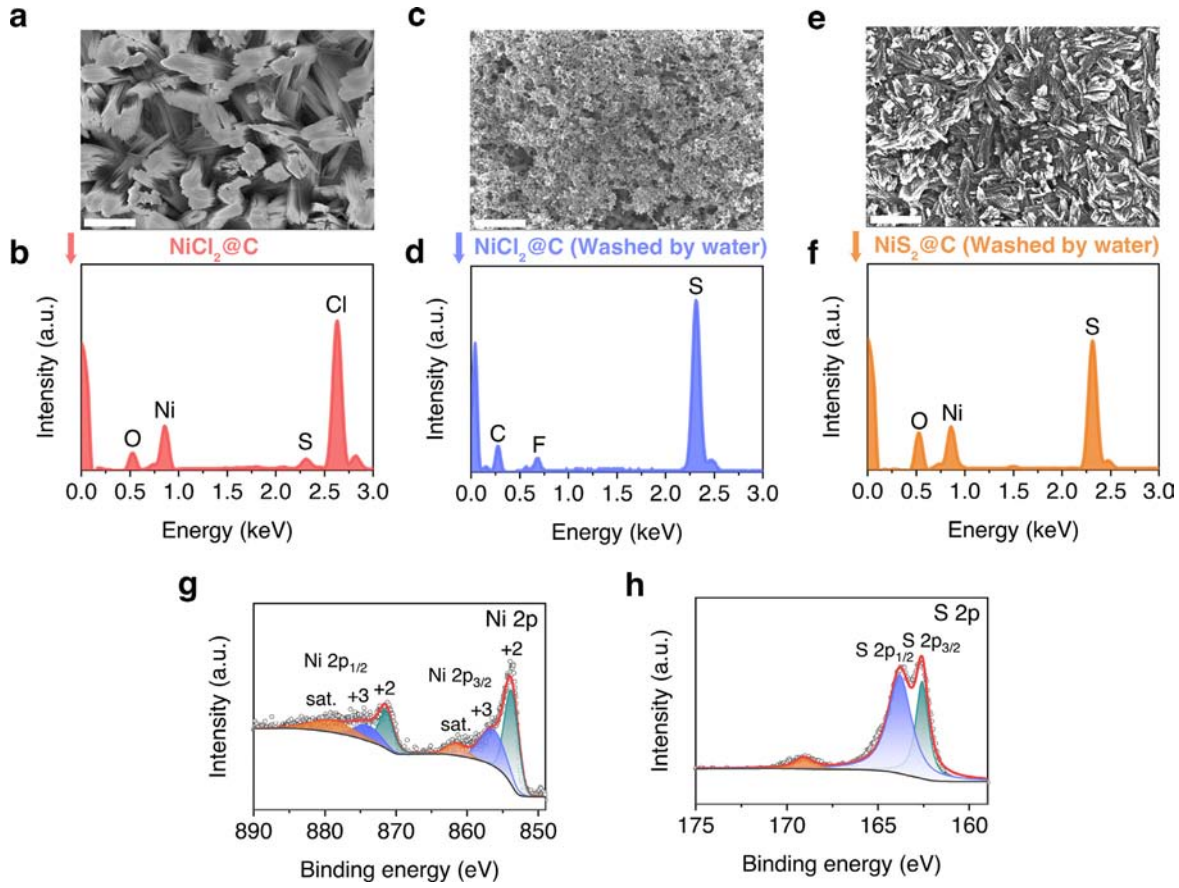

Fig. 2. Characterizations of the cathode precursor and the NiS_2@C cathode. (a) SEM image and (b) corresponding EDX spectrum of the cathode precursor. (c) SEM image and (d) corresponding EDX spectrum of the cathode precursor after being washed by deionized water. (e) SEM image and (f) corresponding EDX spectrum of the NiS_2@C cathode after being washed by deionized water. The scale bars are 2 μm. XPS spectra of (g) Ni 2p and (h) S 2p for the NiS_2@C cathode after being washed by deionized water.

$$3NiS + AlCl_4^- + 2e^- \rightarrow Ni_3S_2 + AlSCl_2^- + 2Cl^- \quad (4b)$$

$$Ni_3S_2 + 2AlCl_4^- + 4e^- \rightarrow 3Ni + 2AlSCl_2^- + 4Cl^- \quad (4c)$$

The full cell reactions in the first discharge can be formulated as:
Cathode:

$$NiS_2 + 2AlCl_4^- + 4e^- \rightarrow Ni + 2AlSCl_2^- + 4Cl^- \quad (4)$$

Anode:

$$Al + 4Cl^- - 3e^- \rightarrow AlCl_4^- \quad (5)$$

Overall:

$$3NiS_2 + 2AlCl_4^- + 4Al + 4Cl^- \rightarrow 3Ni + 6AlSCl_2^- \quad (6)$$

It can be calculated from Fig. 3a that an initial discharging capacity of 840 mAh g^{-1} was achieved (all of the specific capacities of the Al/NiS_2 batteries are calculated based on the weight of NiS_2 used in cathodes). The initial discharging capacity was close to the theoretical specific capacity of NiS_2 (878 mAh g^{-1}), indicating the high productivity of Eq. (3). Meanwhile, specific capacities of 410, 100, and 330 mAh g^{-1} were obtained experimentally at each plateau, respectively, which was in good agreement with the theoretical capacity (439 mAh g^{-1}, 146 mAh g^{-1}, 293 mAh g^{-1}, respectively). The slight differences can be attributed to that part of the NiS was not reduced to Ni_3S_2 but directly transformed into metallic Ni, which was consistent with the XRD results.

Cyclic voltammograms (CV) were used to illustrate the electrochemical performance of the Al/NiS_2 battery after the first discharge. Fig. S8a presents the CV curves of the Mo meshes and Ta wire electrode (Mo/Ta electrode) and the NiS_2@C electrode at a slow scan rate of 0.1 mV s^{-1} from 0 V to 1.5 V. Obvious anodic current signals were detected when the voltage reached 1.05 V in the CV curve of the Mo/Ta electrode, which indicated side reactions (detailed research will be discussed next). As a result, the battery was set to be cycled in the voltage range of 0–1.05 V, where no side reactions occurred (Fig. S8b and S8c). The CV curve of the NiS_2@C electrode presented three obvious oxidation peaks (0.80 V, 0.95 V, and 1.05 V) and three corresponding reduction peaks (0.27 V, 0.58 V, and 0.80 V), demonstrating multi-step reaction mechanisms [44].

The voltage profile of the first charge and the second discharge was also demonstrated in Fig. 3a. The three charge plateaus and three discharge plateaus were in good agreement with the CV curves. Six extra samples labeled from V-X were taken from the cathodes at the end of each voltage plateau and washed by deionized water. The reversibility of the cathode reactions was proved by the XRD tests (Fig. 3c). After the second discharge process, Ni was re-formed at the cathode. It is worth noting that NiS_2 was not detected in sample VII. Instead, Ni_3S_4 was the final charge product, with Ni_3S_2 and β-NiS serving as the intermediate substances. The above conclusions were verified by the XPS and Raman results (Fig. S6c, Fig. S6d, and Fig. S7b). The XPS and Raman spectra of the samples corresponding to the same state of charge/discharge (samples IV&X, samples V&IX, samples VI&VIII) were similar. It is also worth noting that the peak of NiS_2 was not observed in the Raman spectra of sample VII. Therefore, the cathode reactions after the first discharge can

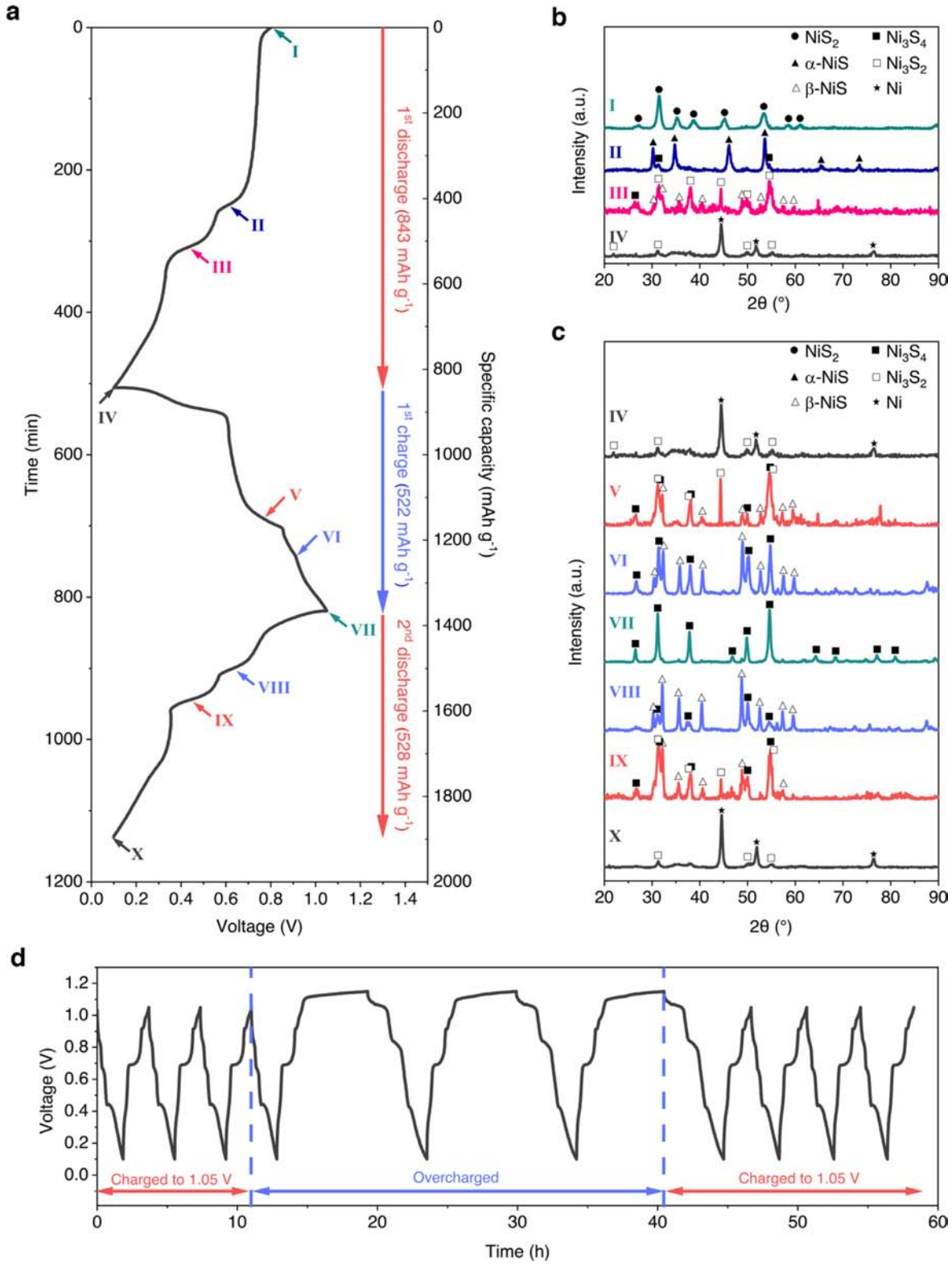

Fig. 3. Electrochemical process and reaction mechanisms of the Al/NiS_2 battery. (a) Voltage profile of the first cycle and the second discharge of the Al/NiS_2 battery cycled at 180 °C and a current density of 100 mA g^{-1}. Ten cathode samples were taken out from the batteries at different stages of charge/discharge and labeled as I to X, respectively. XRD patterns of the cathode samples (b) I-IV and (c) IV-X after being washed by deionized water. (d) Overcharge test of the Al/NiS_2 battery. The battery experienced three overcharged cycles during the cycling process. The current density was 250 mA g^{-1}.

be expressed as follows.

$$Ni_3S_4 + AlCl_4^- + 2e^- \rightleftarrows 3NiS + AlSCl_2^- + 2Cl^- \quad (7a)$$

$$3NiS + AlCl_4^- + 2e^- \rightleftarrows Ni_3S_2 + AlSCl_2^- + 2Cl^- \quad (7b)$$

$$Ni_3S_2 + 2AlCl_4^- + 4e^- \rightleftarrows 3Ni + 2AlSCl_2^- + 4Cl^- \quad (7c)$$

The full cell reactions after the first discharge can be formulated as:
Cathode:

$$Ni_3S_4 + 4AlCl_4^- + 8e^- \rightleftarrows 3Ni + 4AlSCl_2^- + 8Cl^- \quad (7)$$

Anode:

$$Al + 4Cl^- - 3e^- \rightleftarrows AlCl_4^- \quad (8)$$

Overall:

$$3Ni_3S_4 + 4AlCl_4^- + 8Al + 8Cl^- \rightleftarrows 9Ni + 12AlSCl_2^- \quad (9)$$

Since Ni_3S_4, instead of NiS_2, served as the final charge product, the theoretical capacity related to the first discharge plateau in the second and the following cycles (135 mAh g^{-1}) was a third of that in the first cycle. Meanwhile, the discharging capacities related to the other two plateaus remained nearly unchanged because of the same reaction mechanisms.

Cathode samples I, IV, VII, X, and thir corresponding anode samples (labeled as anode samples I, IV, VII, and X) were observed by SEM after being washed by deionized water. It can be seen in Fig. S9 that the active substances of the cathodes were distributed uniformly and adhered tightly to the carbon network. The final discharge product, Ni, showed similar spherical morphologies in cathode samples IV and X. Fig. S10 shows the morphology changes of the Al anode. Pores with diameters of 3–5 μm were formed on the anode surface after the first discharge, indicating the dissolution of Al. Part of the holes were refilled in anode sample VII, which corresponded to the deposition process.

The reaction mechanisms and electrochemical stability of the cell during overcharges were further investigated. The Al/NiS_2 battery experienced three overcharged cycles at 180 °C and a current density of 250 mA g^{-1} (Fig. 3d). A negligible capacity decay was observed after the battery was set back to cycle in the normal voltage range of 0–1.05 V. Fig. S11 shows the charge-discharge curve of an overcharged cycle and a normal cycle. An extra charge plateau existed at 1.09 V. Since Ta and Mo have been repeatedly reported to be electrochemically inert in the non-aqueous AIB systems [45–47], and sulfur was confirmed to be produced on the Mo/Ta electrode by the XRD test (Fig. S12), the corresponding reactions might be the oxidation of $AlSCl_2^-$ ions to sulfur and other polymeric species [48]. The corresponding discharge plateau existed at 1.07 V with a much smaller capacity, mainly because the overcharge products were partly soluble in the electrolyte. It is also worth noting that the discharge plateau at 0.83 V in the overcharged cycle was longer than that in a normal cycle, reflecting changes in cathode reactions. A cathode sample was taken out from the overcharged battery for further investigations. After being washed by deionized water, the sample, labeled as cathode sample XI, was tested by XRD (Fig. S13). Peaks of NiS_2 and Ni_3S_4 were confirmed, which indicated that Ni_3S_4 was further oxidized during the overcharge process. To conclude, since both the electrolyte and the cathode experienced reversible oxidation reactions during the overcharge process, the cycling stability of the battery was not affected.

3.3. Battery performance

Charge-discharge measurements were performed in a voltage range of 0.1–1.05 V for further evaluation of the electrochemical performance of the Al/NiS_2 battery. Fig. S14 shows the charge-discharge curves of the 2nd, 4th, 6th, 8th, and 10th cycles at 180 °C and a current density of 250 mA g^{-1}. The discharging capacity in the 2nd cycle reached 520 mAh g^{-1}, indicating around 90% usage of the active substances supposing Ni_3S_4 to be the final charge product. The voltage hysteresis experienced a noticeable decrease in the first six cycles, which can be attributed to a more uniform distribution of the active substances on carbon black during charge-discharge processes.

Fig. 4a shows the rate performance of the Al/NiS_2 battery at 180 °C, 210 °C, and 240 °C at various current densities ranging from 250 mA g^{-1} to 2000 mA g^{-1}. The battery demonstrated extraordinary rate capability at all working temperatures. Even at a high current density of 2000 mA g^{-1}, the cathode delivered specific capacities of 310 mAh g^{-1}, 365 mAh g^{-1}, and 390 mAh g^{-1} at 180 °C, 210 °C, and 240 °C, respectively. The charge-discharge curves at a current density of 250 mA g^{-1} (Fig. 4b) show that decreased voltage hysteresis and increased specific capacities were achieved at elevated temperatures. Similar results were observed when batteries were cycled at different current densities (Fig. S15).

The Al/NiS_2 battery also demonstrated impressive cycling stability. A cathode capacity of 380 mAh g^{-1} was achieved in the battery system cycled at 180 °C and a current density of 1000 mA g^{-1} after 1000 cycles (Fig. 4c), while a cathode capacity of 320 mAh g^{-1} was achieved in the battery system cycled at 240 °C and a current density of 2000 mA g^{-1} after 2000 cycles (Fig. 4d). Both batteries demonstrated Coulombic efficiencies of nearly 100% and only showed slight capacity fade after the cycling.

The Al/NiS_2 battery showed prominent advantages in terms of cathode capacity, rate capability, and lifetime compared with other high-performance non-aqueous AIBs applying metal sulfide cathodes (Fig. 4e and 4f), which can be mainly attributed to three reasons [19,21,22,29,30,49-51]. Firstly, high electrolyte conductivity and fast reaction kinetics were achieved at high temperatures. Electrochemical impedance spectroscopy (EIS) was conducted, and the Nyquist plots of the Al/NiS_2 battery at different temperatures with the equivalent circuit are shown in Fig. S16. Small electrolyte resistance (1.43 Ω) and charge-transfer resistance (0.62 Ω) were achieved at 180 °C, and both values were further decreased with the temperature (Table S2). Secondly, the NiS_2@C cathode owns high structural stability during cycling. Metal sulfides are commonly synthesized on the nanoscale for room-temperature AIBs [24], which may lead to structural collapse and particle agglomeration. In contrast, the NiS_2@C cathode was prepared in a much simpler way with particle sizes on the micron scale. After being washed by deionized water, the cathode sample taken from the battery cycled at 180 °C for 1000 cycles was observed by SEM (Fig. S17). The active substances of the cathode remained in tight connections with the carbon conductive network, and no apparent grain growth was observed. The XRD results also demonstrated that the final charge and discharge products remained nearly unchanged after cycling, except some intermediate products were not fully involved in the reaction (Fig. S18 and Fig. S19). Thirdly, it has been reported that metal sulfide cathodes may experience decomposition and dissolution in chloroaluminate-based ILs [27,52,53]. However, the cathode materials at different states of charge/discharge were confirmed to be insoluble in the electrolyte (Table S3). It is worth noting that the results above also proved the necessity of synthesizing the sulfide cathode since $NiCl_2$ is partially soluble in NaCl-$AlCl_3$ melts (Table S4). A battery using $NiCl_2$@C cathode and NaCl-saturated NaCl-$AlCl_3$ melts electrolyte was assembled for comparisons (Fig. S20). The initial cathode capacity was 410 mAh g^{-1} based on the weight of $NiCl_2$ used in the cathode, which almost reached the theoretical value (416 mAh g^{-1}). However, the capacity decayed rapidly to 160 mAh g^{-1} after 20 cycles.

As seen in Table S5, the intermediate-temperature Al/NiS_2 battery also demonstrated higher mass energy density (204 Wh kg^{-1}) and volumetric energy density (673 Wh L^{-1}) with lower raw material cost (28 \$ kWh^{-1}) comparable to AIBs with graphite cathodes (67 Wh kg^{-1}, 101 Wh L^{-1}, and 530 \$ kWh^{-1}). The Al/NiS_2 battery owns higher energy densities because of the high capacities of both the cathode and the anode. It is noteworthy that the Al/NiS_2 battery is assembled in the charged state, while the Al/$AlCl_3$-[EMI*m*]Cl/graphite

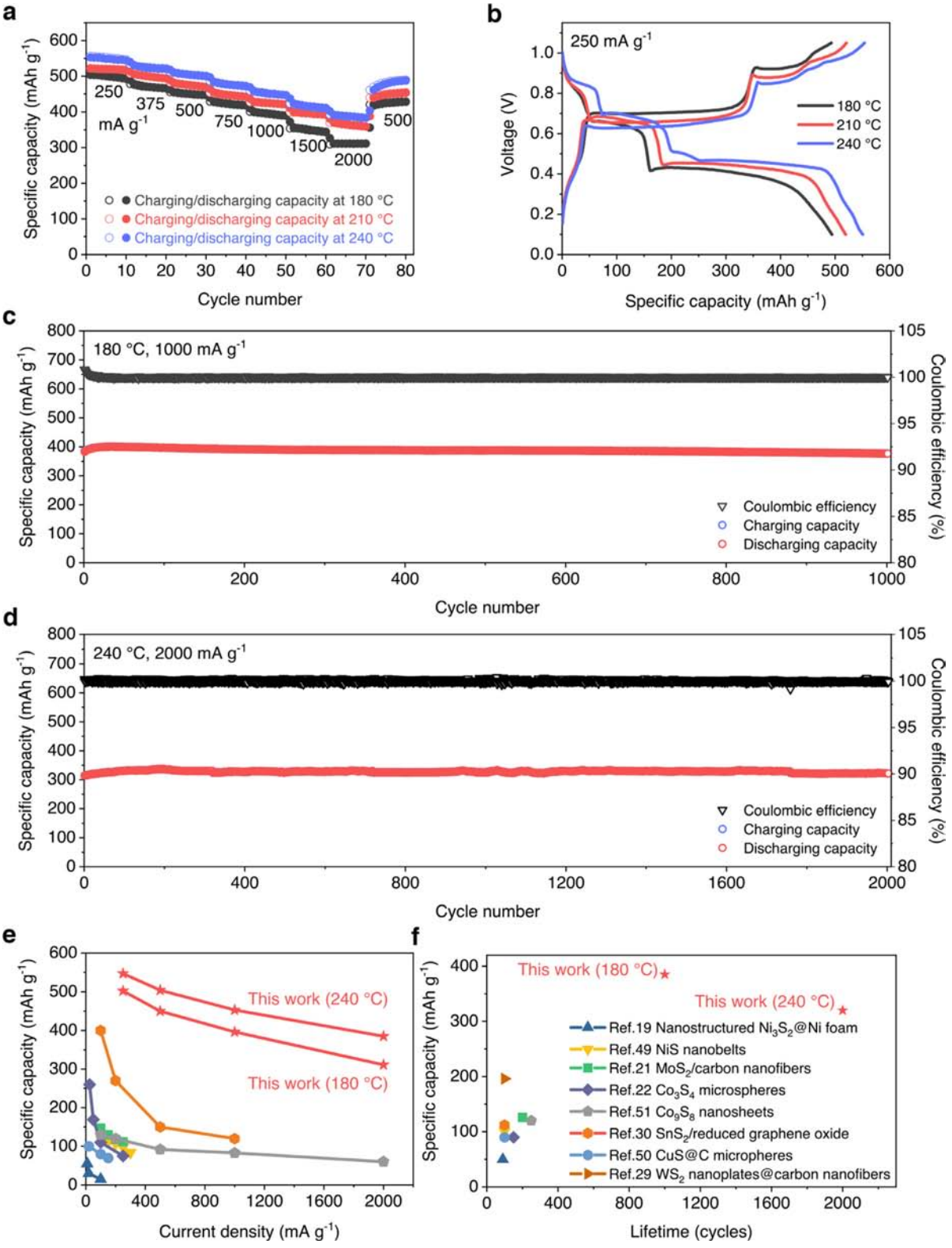

Fig. 4. Electrochemical performance of the Al/NiS_2 battery. (a) Specific capacities at different current densities ranging from 250 mA g^{-1} to 2000 mA g^{-1} at 180 °C, 210 °C, and 240 °C. (b) Charge-discharge curves at a current density of 250 mA g^{-1} at 180 °C, 210 °C, and 240 °C. (c) Cycling performance over 1000 cycles at 180 °C and a current density of 1000 mA g^{-1}. (d) Cycling performance over 2000 cycles at 240 °C and a current density of 2000 mA g^{-1}. (e, f) Comparisons of the Al/NiS_2 battery with other high-performance non-aqueous AIBs applying metal sulfide cathodes in terms of cathode capacity, rate capability, and lifetime [19,21,22,29,30,49–51].

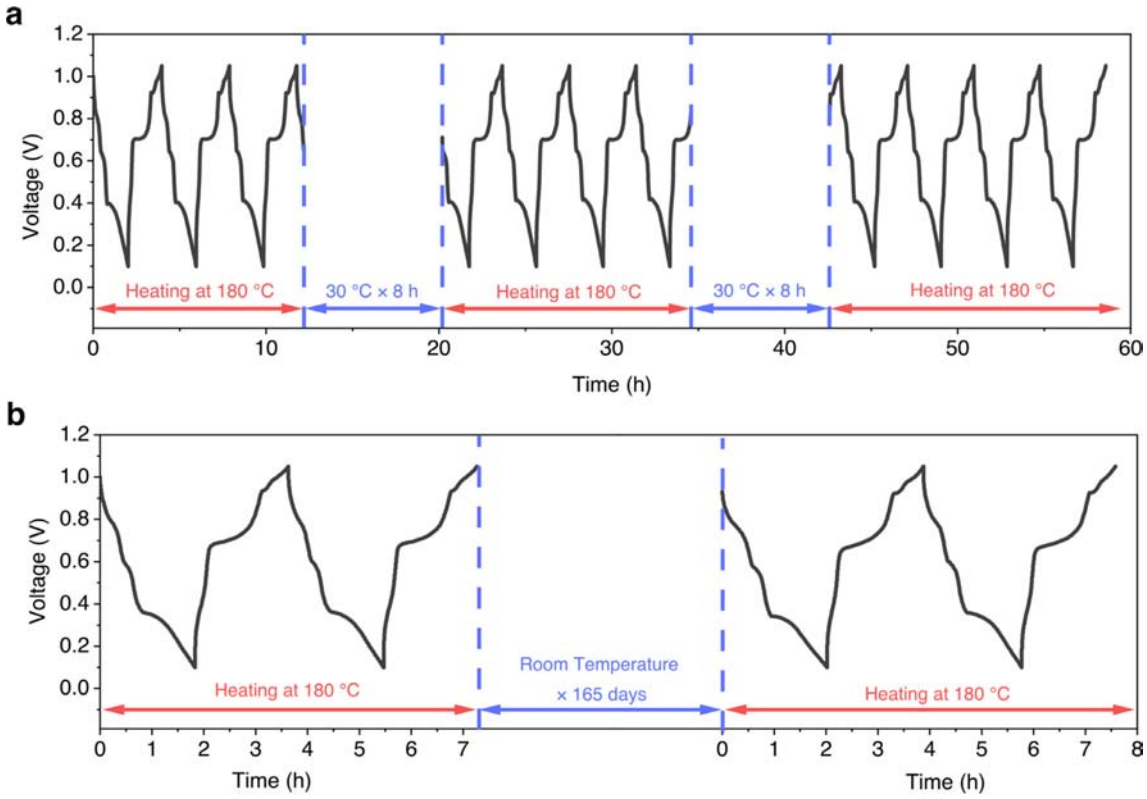

Fig. 5. Freezing-thawing tests of the Al/NiS_2 battery. (a) The battery was terminated and cooled down to 30 °C for 8 h during a charge and a discharge process. The current density was 250 mA g^{-1}. (b) After being charged to 1.05 V, the battery was terminated, cooled down, and kept at room temperature for 165 days. Then the battery was heated to 180 °C and restarted.

battery is assembled in the discharged state. For the former, NiS_2 (~550 mAh g^{-1}) serves as the cathode, metal Al (2978 mAh g^{-1}) serves as the anode, and the molten salt electrolyte is not the active substance in the electrochemical reactions. For the latter, graphite (~120 mAh g^{-1}) serves as the cathode, and $AlCl_3$ can be considered the actual anode material. As a result, a large amount of IL should be added, leading to low anode capacities (<46 mAh g^{-1}) [54–56]. Moreover, the raw material cost of Al/$AlCl_3$-[EMI*m*]Cl/graphite battery is much higher because of the application of the IL electrolyte (48.6 $ kg^{-1}, comparable to 0.7 $ kg^{-1} for the inorganic molten salt electrolyte).

To conclude, the Al/NiS_2 battery demonstrated superior electrochemical performance with lower raw material cost over ambient-temperature non-aqueous Al-ion batteries. Compared with other high-temperature battery systems, the Al/NiS_2 battery can provide higher security because of the relatively low working temperature and the absence of molten alkali metals (Table S6) [57–59]. In addition, although the energy densities of the Al/NiS_2 battery are lower than those of the high-temperature Na/$NiCl_2$ battery and Li/$ZnCl_2$ battery systems, applying the molten salt electrolyte instead of ceramic electrolytes makes the battery system more suitable for large-scale applications [58,59].

Reliable and affordable electricity systems based on wind and solar may depend on the ability to store large quantities of low-cost energy over long timescales [60]. Although long-duration energy storage is urgently desired for the deployment of low-carbon grids in recent years, few technologies have succeeded at scale [61,62]. Our intermediate-temperature Al/NiS_2 battery, however, may be a promising candidate for long-duration energy storage for two reasons. Firstly, the material cost of the battery system is relatively low, which means the installed energy capital costs can be reduced to an acceptable level. Secondly, the battery can be kept at room temperature to avoid self-discharge and reduce maintenance costs. As seen in Fig. 5a, the battery was terminated and cooled down to 30 °C for 8 h during a charge and a discharge process. When the working temperature returned to 180 °C, the cell worked normally with no open nor short circuits, and no significant capacity decay was observed. Meanwhile, in Fig. 5b, after being charged to 1.05 V and kept at room temperature for over 5 months, the battery could be restarted and showed negligible self-discharge. Therefore, the battery system can be charged at working temperatures and store energy over long timescales without self-discharge at ambient temperature, which provides a new scheme for long-duration energy storage with low cost, high safety, and high reliability.

4. Conclusions

Our work develops an intermediate-temperature AIB based on the NiS_2@C cathode and the NaCl-$AlCl_3$-Al_2S_3 molten salt electrolyte. The multi-step conversion between Ni_3S_4 and Ni is clarified and applied as cathode reactions. The battery system shows broad prospects for large-scale applications. Firstly, applying the inorganic molten salt electrolyte instead of the IL electrolyte reduces the material cost, while applying the in-situ molten salt synthesis method for cathode preparation reduces the manufacturing cost. Secondly, the battery system has a competitive theoretical energy density of 204 Wh kg^{-1} and 673 Wh L^{-1}. Experimentally, an ultrahigh cathode capacity of over 500 mAh g^{-1} is obtained. The full cell also shows excellent overall performance. A cathode capacity of 320 mAh g^{-1} is achieved in the battery cycled at 240 °C and a current density of 2000 mA g^{-1} after 2000 cycles. Thirdly, the stability against overcharges and the ability to recover from frozen states of the battery system guarantee high robustness during operations. Overall, the low cost, high safety, and stable electrochemical performance of the Al/NiS_2 battery system make it a promising candidate for future concentrated and large-scale energy storage applications.

Declaration of Competing Interest

The authors declare that they have no known competing financial interests or personal relationships that could have appeared to influence the work reported in this paper.

Data Availability

The data that support the findings of this study are available from the corresponding author upon reasonable request.

CRediT authorship contribution statement

Kuangyu Wang: Conceptualization, Formal analysis, Investigation, Writing – original draft, Writing – review & editing. **Kai Liu:** Conceptualization, Formal analysis, Writing – original draft, Writing – review & editing. **Cheng Yang:** Investigation, Writing – original draft. **Ziyao Chen:** Investigation, Writing – original draft. **Haitian Zhang:** Investigation, Writing – original draft. **Yulong Wu:** Investigation, Writing – original draft. **Yuanzheng Long:** Investigation, Writing – original draft. **Yang Jin:** Writing – original draft, Writing – review & editing. **Xiangming He:** Writing – original draft, Writing – review & editing. **Meicheng Li:** Writing – review & editing. **Hui Wu:** Conceptualization, Formal analysis, Writing – original draft, Writing – review & editing, Supervision, Project administration.

Acknowledgements

This work was supported by the Basic Science Center Program of the National Natural Science Foundation of China (NSFC) under Grant No. 51788104, and Beijing Natural Science Foundation under Grant No. JQ19005.

Supplementary materials

Supplementary material associated with this article can be found, in the online version, at doi:10.1016/j.ensm.2022.03.030.

References

[1] B. Dunn, H. Kamath, J.-.M. Tarascon, Electrical energy storage for the grid: a battery of choices, Science 334 (2011) 928–935, doi:10.1126/science.1212741.
[2] L. Xu, Y. Lu, C. Zhao, H. Yuan, G. Zhu, L. Hou, Q. Zhang, J. Huang, Toward the scale-up of solid-state lithium metal batteries: the gaps between lab-level cells and practical large-format batteries, Adv. Energy Mater. 11 (2021) 2002360, doi:10.1002/aenm.202002360.
[3] D. Wang, W. Zhang, W. Zheng, X. Cui, T. Rojo, Q. Zhang, Towards high-safe lithium metal anodes: suppressing lithium dendrites via tuning surface energy, Adv. Sci. 4 (2017) 1600168, doi:10.1002/advs.201600168.
[4] G. Martin, L. Rentsch, M. Höck, M. Bertau, Lithium market research – global supply, future demand and price development, Energy Storage Mater 6 (2017) 171–179, doi:10.1016/j.ensm.2016.11.004.
[5] M. Walter, M.V. Kovalenko, K.V. Kravchyk, Challenges and benefits of post-lithium-ion batteries, New J. Chem. 44 (2020) 1677–1683, doi:10.1039/C9NJ05682C.
[6] L. Wang, Y. Lu, J. Liu, M. Xu, J. Cheng, D. Zhang, J.B. Goodenough, A superior low-cost cathode for a Na-ion battery, Angew. Chemie. 125 (2013) 2018–2021, doi:10.1002/ange.201206854.
[7] F. Wang, X. Fan, T. Gao, W. Sun, Z. Ma, C. Yang, F. Han, K. Xu, C. Wang, High-voltage aqueous magnesium ion batteries, ACS Cent. Sci. 3 (2017) 1121–1128, doi:10.1021/acscentsci.7b00361.
[8] M. Lin, M. Gong, B. Lu, Y. Wu, D. Wang, M. Guan, M. Angell, C. Chen, J. Yang, B. Hwang, H. Dai, An ultrafast rechargeable aluminium-ion battery, Nature 520 (2015) 324–328, doi:10.1038/nature14340.
[9] S.K. Das, S. Mahapatra, H. Lahan, Aluminium-ion batteries: developments and challenges, J. Mater. Chem. A. 5 (2017) 6347–6367, doi:10.1039/C7TA00228A.
[10] K. Liang, L. Ju, S. Koul, A. Kushima, Y. Yang, Self-supported tin sulfide porous films for flexible aluminum-ion batteries, Adv. Energy Mater. 9 (2019) 1802543, doi:10.1002/aenm.201802543.
[11] K. Zhang, K.O. Kirlikovali, J.M. Suh, J.W. Choi, H.W. Jang, R.S. Varma, O.K. Farha, M. Shokouhimehr, Recent advances in rechargeable aluminum-ion batteries and considerations for their future progress, ACS Appl. Energy Mater. 3 (2020) 6019–6035, doi:10.1021/acsaem.0c00957.
[12] H. Zhang, X. Liu, H. Li, I. Hasa, S. Passerini, Challenges and strategies for high-energy aqueous electrolyte rechargeable batteries, Angew. Chemie Int. Ed. 60 (2021) 598–616, doi:10.1002/anie.202004433.
[13] G.A. Elia, K.V. Kravchyk, M.V. Kovalenko, J. Chacón, A. Holland, R.G.A. Wills, An overview and prospective on Al and Al-ion battery technologies, J. Power Sources. 481 (2021) 228870, doi:10.1016/j.jpowsour.2020.228870.
[14] S. Jiao, H. Lei, J. Tu, J. Zhu, J. Wang, X. Mao, An industrialized prototype of the rechargeable Al/$AlCl_3$-[EMIm]Cl/graphite battery and recycling of the graphitic cathode into graphene, Carbon N Y 109 (2016) 276–281, doi:10.1016/j.carbon.2016.08.027.
[15] K.V. Kravchyk, S. Wang, L. Piveteau, M.V. Kovalenko, Efficient aluminum chloride-natural graphite battery, Chem. Mater. 29 (2017) 4484–4492, doi:10.1021/acs.chemmater.7b01060.
[16] E. Zhang, J. Wang, B. Wang, X. Yu, H. Yang, B. Lu, Unzipped carbon nanotubes for aluminum battery, Energy Storage Mater 23 (2019) 72–78, doi:10.1016/j.ensm.2019.05.030.
[17] E. Faegh, B. Ng, D. Hayman, W.E. Mustain, Practical assessment of the performance of aluminium battery technologies, Nat. Energy. 6 (2021) 21–29, doi:10.1038/s41560-020-00728-y.
[18] S. Wang, Z. Yu, J. Tu, J. Wang, D. Tian, Y. Liu, S. Jiao, A novel aluminum-ion battery: Al/$AlCl_3$-[EMIm]Cl/Ni_3S_2@Graphene, Adv. Energy Mater. 6 (2016) 1600137, doi:10.1002/aenm.201600137.
[19] Z. Li, C. Gao, J. Zhang, A. Meng, H. Zhang, L. Yang, Mountain-like nanostructured 3D Ni_3S_2 on Ni foam for rechargeable aluminum battery and its theoretical analysis on charge/discharge mechanism, J. Alloys Compd. 798 (2019) 500–506, doi:10.1016/j.jallcom.2019.05.270.
[20] Z. Li, B. Niu, J. Liu, J. Li, F. Kang, Rechargeable aluminum-ion battery based on MoS_2 microsphere cathode, ACS Appl. Mater. Interfaces. 10 (2018) 9451–9459, doi:10.1021/acsami.8b00100.
[21] W. Yang, H. Lu, Y. Cao, B. Xu, Y. Deng, W. Cai, Flexible free-standing MoS_2/carbon nanofibers composite cathode for rechargeable aluminum-ion batteries, ACS Sustain. Chem. Eng. 7 (2019) 4861–4867, doi:10.1021/acssuschemeng.8b05292.
[22] H. Li, H. Yang, Z. Sun, Y. Shi, H. Cheng, F. Li, A highly reversible Co_3S_4 microsphere cathode material for aluminum-ion batteries, Nano Energy 56 (2019) 100–108, doi:10.1016/j.nanoen.2018.11.045.
[23] Y. Hu, D. Ye, B. Luo, H. Hu, X. Zhu, S. Wang, L. Li, S. Peng, L. Wang, A binder-free and free-standing cobalt sulfide@carbon nanotube cathode material for aluminum-ion batteries, Adv. Mater. 30 (2018) 1703824, doi:10.1002/adma.201703824.
[24] L. Xing, K.A. Owusu, X. Liu, J. Meng, K. Wang, Q. An, L. Mai, Insights into the storage mechanism of VS_4 nanowire clusters in aluminum-ion battery, Nano Energy 79 (2021) 105384, doi:10.1016/j.nanoen.2020.105384.
[25] X. Zhang, S. Wang, J. Tu, G. Zhang, S. Li, D. Tian, S. Jiao, Flower-like vanadium sulfide/reduced graphene oxide composite: an energy storage material for aluminum-ion batteries, ChemSusChem 11 (2018) 709–715, doi:10.1002/cssc.201702270.
[26] H. Wang, S. Chen, C. Fu, Y. Ding, G. Liu, Y. Cao, Z. Chen, Recent advances in conversion-type electrode materials for post lithium-ion batteries, ACS Mater. Lett. 3 (2021) 956–977, doi:10.1021/acsmaterialslett.1c00043.
[27] S. Chen, D. Zhao, L. Chen, G. Liu, Y. Ding, Y. Cao, Z. Chen, Emerging intercalation cathode materials for multivalent metal-ion batteries: status and challenges, Small Struct 2 (2021) 2100082, doi:10.1002/sstr.202100082.
[28] Y. Zhang, S. Liu, Y. Ji, J. Ma, H. Yu, Emerging nonaqueous aluminum-ion batteries: challenges, status, and perspectives, Adv. Mater. 30 (2018) 1706310, doi:10.1002/adma.201706310.
[29] W. Yang, H. Lu, Y. Cao, P. Jing, Single-/few-layered ultrasmall WS_2 nanoplates embedded in nitrogen-doped carbon nanofibers as a cathode for rechargeable aluminum batteries, J. Power Sources. 441 (2019) 227173, doi:10.1016/j.jpowsour.2019.227173.
[30] Y. Hu, B. Luo, D. Ye, X. Zhu, M. Lyu, L. Wang, An innovative freeze-dried reduced graphene oxide supported SnS_2 cathode active material for aluminum-ion batteries, Adv. Mater. 29 (2017) 1606132, doi:10.1002/adma.201606132.
[31] H.A. Hjuler, R.W. Berg, K. Zachariassen, N.J. Bjerrum, Specific conductivity of NaCl-$AlCl_3$ and NaCl-$AlCl_3$-Al_2S_3 melts, J. Chem. Eng. Data. 30 (1985) 203–208, doi:10.1021/je00040a022.
[32] V.A. Elterman, P.Y. Shevelin, L.A. Yolshina, E.G. Vovkotrub, A.V. Borozdin, Effects of $AlCl_3$-1-ethyl-3-methylimidazolium chloride ionic liquid composition on transport properties, J. Mol. Liq. 320 (2020) 114482, doi:10.1016/j.molliq.2020.114482.
[33] K. Wang, K. Jiang, B. Chung, T. Ouchi, P.J. Burke, D.A. Boysen, D.J. Bradwell, H. Kim, U. Muecke, D.R. Sadoway, Lithium–antimony–lead liquid metal battery for grid-level energy storage, Nature 514 (2014) 348–350, doi:10.1038/nature13700.
[34] Y. Huang, C. Yang, B. Deng, C. Wang, Q. Li, C. De Villenoisy Thibault, K. Huang, K. Huo, H. Wu, Nanostructured pseudocapacitors with pH-tunable electrolyte for electrochromic smart windows, Nano Energy 66 (2019) 104200, doi:10.1016/j.nanoen.2019.104200.
[35] N. Takami, N. Koura, Anodic sulfidation of FeS electrode in a NaCl saturated $AlCl_3$-NaCl melt, Electrochim. Acta. 33 (1988) 1137–1142, doi:10.1016/0013-4686(88)80205-6.
[36] R.W. Berg, S. Von Winbush, N.J. Bjerrum, Negative oxidation states of the chalcogens in molten salts. 1. Raman spectroscopic studies on aluminum chlorosulfides formed in chloride and chloroaluminate melts and some related solid and dissolved compounds, Inorg. Chem. 19 (1980) 2688–2698, doi:10.1021/ic50211a042.
[37] T. Tian, L. Huang, L. Ai, J. Jiang, Surface anion-rich NiS_2 hollow microspheres derived from metal-organic frameworks as a robust electrocatalyst for the hydrogen evolution reaction, J. Mater. Chem. A. 5 (2017) 20985–20992, doi:10.1039/c7ta06671f.
[38] H. Wang, M. Liang, D. Duan, W. Shi, Y. Song, Z. Sun, Rose-like Ni_3S_4 as battery-type electrode for hybrid supercapacitor with excellent charge storage performance, Chem. Eng. J. 350 (2018) 523–533, doi:10.1016/j.cej.2018.05.004.

[39] B. Guan, Y. Li, B. Yin, K. Liu, D. Wang, H. Zhang, C. Cheng, Synthesis of hierarchical NiS microflowers for high performance asymmetric supercapacitor, Chem. Eng. J. 308 (2017) 1165–1173, doi:10.1016/j.cej.2016.10.016.
[40] X. Ao, Z. Wen, X. Wu, T. Wu, M. Wu, Self-repairing function of Ni_3S_2 layer on Ni particles in the Na/$NiCl_2$ cells with the addition of sulfur in the catholyte, ACS Appl. Mater. Interfaces. 9 (2017) 21234–21242, doi:10.1021/acsami.7b03873.
[41] A.N. Mansour, Characterization of NiO by XPS, Surf. Sci. Spectra. 3 (1994) 231–238, doi:10.1116/1.1247751.
[42] T. Suzuki, K. Uchinokura, T. Sekine, E. Matsuura, Raman scattering of NiS_2, Solid State Commun 23 (1977) 847–852, doi:10.1016/0038-1098(77)90967-X.
[43] D.W. Bishop, P.S. Thomas, A.S. Ray, Raman spectra of nickel(II) sulfide, Mater. Res. Bull. 33 (1998) 1303–1306, doi:10.1016/S0025-5408(98)00121-4.
[44] X. Pu, D. Zhao, C. Fu, Z. Chen, S. Cao, C. Wang, Y. Cao, Understanding and calibration of charge storage mechanism in cyclic voltammetry curves, Angew. Chemie. 133 (2021) 21480–21488, doi:10.1002/ange.202104167.
[45] Z. Zhao, Z. Hu, H. Liang, S. Li, H. Wang, F. Gao, X. Sang, H. Li, Nanosized $MoSe_2$@carbon matrix: a stable host material for the highly reversible storage of potassium and aluminum ions, ACS Appl. Mater. Interfaces. 11 (2019) 44333–44341, doi:10.1021/acsami.9b16155.
[46] J. Zheng, D.C. Bock, T. Tang, Q. Zhao, J. Yin, K.R. Tallman, G. Wheeler, X. Liu, Y. Deng, S. Jin, A.C. Marschilok, E.S. Takeuchi, K.J. Takeuchi, L.A. Archer, Regulating electrodeposition morphology in high-capacity aluminium and zinc battery anodes using interfacial metal–substrate bonding, Nat. Energy. 6 (2021) 398–406, doi:10.1038/s41560-021-00797-7.
[47] Y. Song, S. Jiao, J. Tu, J. Wang, Y. Liu, H. Jiao, X. Mao, Z. Guo, D.J. Fray, A long-life rechargeable Al ion battery based on molten salts, J. Mater. Chem. A. 5 (2017) 1282–1291, doi:10.1039/C6TA09829K.
[48] N.Q. Minh, R.O. Loutfy, N.P. Yao, A preliminary study of the electrolysis of aluminum sulfide in molten salts, 1983.
[49] Z. Yu, Z. Kang, Z. Hu, J. Lu, Z. Zhou, S. Jiao, Hexagonal NiS nanobelts as advanced cathode materials for rechargeable Al-ion batteries, Chem. Commun. 52 (2016) 10427–10430, doi:10.1039/C6CC05974K.
[50] S. Wang, S. Jiao, J. Wang, H. Chen, D. Tian, H. Lei, D. Fang, High-performance aluminum-ion battery with CuS@C microsphere composite cathode, ACS Nano 11 (2017) 469–477, doi:10.1021/acsnano.6b06446.
[51] Z. Hu, K. Zhi, Q. Li, Z. Zhao, H. Liang, X. Liu, J. Huang, C. Zhang, H. Li, X. Guo, Two-dimensionally porous cobalt sulfide nanosheets as a high-performance cathode for aluminum-ion batteries, J. Power Sources. 440 (2019) 227147, doi:10.1016/j.jpowsour.2019.227147.
[52] W. Xing, X. Li, T. Cai, Y. Zhang, P. Bai, J. Xu, H. Hu, M. Wu, Q. Xue, Y. Zhao, J. Zhou, S. Zhuo, X. Gao, Z. Yan, Layered double hydroxides derived NiCo-sulfide as a cathode material for aluminum ion batteries, Electrochim. Acta. 344 (2020) 136174, doi:10.1016/j.electacta.2020.136174.
[53] Z. Zhao, Z. Hu, R. Jiao, Z. Tang, P. Dong, Y. Li, S. Li, H. Li, Tailoring multi-layer architectured FeS_2@C hybrids for superior sodium-, potassium- and aluminum-ion storage, Energy Storage Mater 22 (2019) 228–234, doi:10.1016/j.ensm.2019.01.022.
[54] A. Bakkar, V. Neubert, A new method for practical electrodeposition of aluminium from ionic liquids, Electrochem. Commun. 51 (2015) 113–116, doi:10.1016/j.elecom.2014.12.012.
[55] A.P. Abbott, R.C. Harris, Y.T. Hsieh, K.S. Ryder, I.W. Sun, Aluminium electrodeposition under ambient conditions, Phys. Chem. Chem. Phys. 16 (2014) 14675–14681, doi:10.1039/c4cp01508h.
[56] Y. Fang, K. Yoshii, X. Jiang, X.G. Sun, T. Tsuda, N. Mehio, S. Dai, An $AlCl_3$ based ionic liquid with a neutral substituted pyridine ligand for electrochemical deposition of aluminum, Electrochim. Acta. 160 (2015) 82–88, doi:10.1016/j.electacta.2015.02.020.
[57] H. Yin, B. Chung, F. Chen, T. Ouchi, J. Zhao, N. Tanaka, D.R. Sadoway, Faradaically selective membrane for liquid metal displacement batteries, Nat. Energy. 3 (2018) 127–131, doi:10.1038/s41560-017-0072-1.
[58] K. Liu, J. Lang, M. Yang, J. Xu, B. Sun, Y. Wu, K. Wang, Z. Zheng, Z. Huang, C. Wang, H. Wu, Y. Jin, Y. Cui, Molten lithium-brass/zinc chloride system as high-performance and low-cost battery, Matter 3 (2020) 1–11, doi:10.1016/j.matt.2020.08.022.
[59] K.B. Hueso, M. Armand, T. Rojo, High temperature sodium batteries: status, challenges and future trends, Energy Environ. Sci. 6 (2013) 734–749, doi:10.1039/c3ee24086j.
[60] J.A. Dowling, K.Z. Rinaldi, T.H. Ruggles, S.J. Davis, M. Yuan, F. Tong, N.S. Lewis, K. Caldeira, Role of long-duration energy storage in variable renewable electricity systems, Joule 4 (2020) 1907–1928, doi:10.1016/j.joule.2020.07.007.
[61] O.J. Guerra, J. Zhang, J. Eichman, P. Denholm, J. Kurtz, B.-.M. Hodge, The value of seasonal energy storage technologies for the integration of wind and solar power, Energy Environ. Sci. 13 (2020) 1909–1922, doi:10.1039/D0EE00771D.
[62] P. Albertus, J.S. Manser, S. Litzelman, Long-duration electricity storage applications, economics, and technologies, Joule 4 (2020) 21–32, doi:10.1016/j.joule.2019.11.009.